New radio-frequency setup for studying large 2D complex plasma crystals

V. Nosenko,[1, a)] J. Meyer,[1] S. K. Zhdanov,[1] and H. M. Thomas[1]
[1] *Institut für Materialphysik im Weltraum, Deutsches Zentrum für Luft- und Raumfahrt (DLR), D-82234 Weßling, Germany*

(Dated: 20 November 2018)

Complex plasma crystals are popular model systems where various plasma-specific or generic phenomena can be studied at the level of individual particles. Addressing the growing need for larger two-dimensional (2D) plasma crystals, a new plasma setup was built at the DLR Institute of Materials Physics in Space. The setup allows obtaining larger than before, highly ordered 2D plasma crystals and exploring new parameter ranges. It is based on a relatively large (90 cm in diameter) vacuum chamber where a capacitively coupled radio-frequency discharge is used to levitate polymer microparticles. The discharge is created between the lower rf electrode and the grounded chamber walls, the particles levitate in the plasma (pre)sheath above the electrode and are observed by video microscopy through the large top glass window and through the side windows. The first observations of plasma crystals in the new setup are reported.

PACS numbers: 52.80.Pi, 52.75.-d, 52.27.Lw, 52.35.Fp

I. INTRODUCTION

Complex, or dusty plasmas are suspensions of fine solid particles in a weakly ionized gas[1]. The particles charge up by collecting electrons and ions from the plasma and can be confined in the plasma regions where their weight is balanced by other forces, e.g. electrostatic force. Due to the interplay between their mutual interactions and external confinement, the particles can form various structures which are often strongly coupled and possess liquid-like or even solid-like order. The crystalline phase of complex plasma is called the plasma crystal[2–4]. In laboratory experiments with monodisperse particles, single-layer (2D) plasma crystals can be obtained[5–8]. Complex plasmas are popular versatile model systems that are used to simulate the structure and dynamic processes in regular liquids and solids. With microparticles serving as proxy "atoms," they offer the benefit of real-time direct imaging of various processes at the "atomistic" level. Examples include the studies of waves[6–9], phase transitions[10–12], and transport phenomena[13–17] in complex plasmas.

There is a growing body of evidence that many properties of complex plasmas, such as thermal conductivity and diffusion coefficient may be system-size dependent. To test this assumption, experiments are needed where the size of a complex plasma can be varied in a wide range. So far, the existing experimental setups (based on various modifications of the GEC rf reference cell[18]) allowed the maximum size of a high-quality 2D plasma crystal of about $6-7$ cm. To obtain much larger uniform 2D plasma crystals, a larger setup is necessary. In this paper, we report on the new radio-frequency setup that has been built and is now operational at the DLR Institute of Materials Physics in Space. It is based on a relatively large vacuum chamber (with the external diameter of 90 cm) and allows obtaining larger than before 2D complex plasma crystals. The first observations of plasma crystals in the new setup are reported.

II. NEW COMPLEX-PLASMA SETUP

A. Hardware solutions and data analysis method

The central part of the setup is a large vacuum chamber, which is a stainless steel cylinder 90 cm in diameter and 34 cm in height with upper and lower flanges, 36 cm diameter glass window in the center of the upper flange, and multiple smaller top and side viewports, see Fig. 1. It is pumped by one of two turbo pumps, Oerlikon Leybold Turbovac MAG W 1300 iPL or Oerlikon Leybold Turbovac SL300 with the pumping rates of 1100 l/s or 270 l/s, respectively. Both pumps employ magnetic rotor levitation, water cooling, and are oil-free. The turbo pumps are backed by the Oerlikon Leybold Scrollvac SC 30D roughing pump, which is also oil-free. Two gate valves which are actuated pneumatically are used to separate the pumps from the vacuum chamber. Inert gas (currently argon) is admitted into the chamber through a flow controller (MKS 1179BX) while the pumping speed is regulated by a butterfly valve (MKS 653B) installed in the smaller turbo pump contour to set a desired gas pressure. The gas pressure in the chamber is measured by the Ionivac ITR 90 gauge coupled with the Combivac IT23 read-out and the MKS Baratron 722B gauge coupled with MKS PR 4000 read-out.

Capacitively coupled rf plasma is sustained by a 13.56-MHz rf generator (Dressler Ceasar 133) paired with automatic matching unit (Adtec AMV-300S). A 77.5 cm diameter aluminium-alloy disc positioned at about half of the chamber height serves as the powered rf electrode, with the chamber walls and the upper flange acting as the grounded electrode. The rf electrode can be actively

[a)] Electronic mail: V.Nosenko@dlr.de

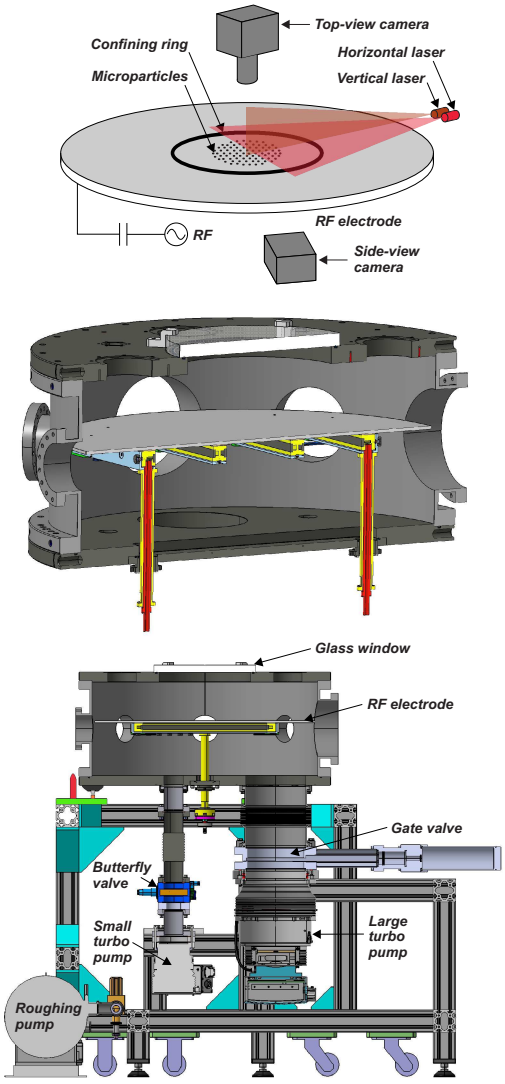

FIG. 1. Experimental setup for studying large 2D complex plasma crystals. Plasma is produced by a capacitively coupled rf discharge in argon. (upper panel) Polymer microspheres are levitated against gravity in the plasma (pre)sheath above the lower rf electrode. The particles are illuminated with two lasers and are imaged from the top and from the side by two video cameras. (middle panel) The vacuum chamber is a stainless-steel cylinder 90 cm in diameter and 34 cm in height with ports for imaging and measurements. The powered rf electrode is a 77.5 cm diameter aluminium-alloy disc with the upper flange and chamber walls serving as the grounded electrode. (lower panel) Overall layout of the setup where the main vacuum components are shown. The vacuum chamber rests on three supports with adjustable heights, so that the whole chamber tilt can be adjusted.

cooled by running water; however, for the rf power range used in this paper this was not necessary.

A manual particle dispenser mounted in the upper flange is used to inject dust particles into the plasma. The particle dispenser is a small aluminium-alloy container with an internal cylindrical cut-out (diameter of 0.8 cm) where a load of particles is placed. The bottom part of the cut-out is covered with a metal sieve with the opening size of 15 μm. When the dispenser is agitated, the particles leave it through the sieve. This helps to prevent the particle agglomeration. Melamine formaldehyde microspheres[19] with a diameter of 9.19 ± 0.09 μm are currently used.

The particles are suspended in the plasma sheath above the rf electrode. They are illuminated by a horizontal laser sheet with the wavelength $\lambda = 660$ nm and maximum output power of 100 mW. A vertical laser sheet with $\lambda = 635$ nm is used for illuminating a desired vertical cross-section of the particle suspension.

The particles are imaged from above using one of the following combinations of cameras and lenses. First, the Photron FASTCAM mini WX100 camera equipped with either the Nikon AF-95S VR Micro-Nikkor 105-mm lens or a long-distance microscope Questar QM100. The Photron camera has a high maximum frame rate of 1080 frames per second (fps) at full resolution but a limited on-board memory and therefore limited duration of recorded video. Second, Ximea xiQ MQ042MG-CM camera equipped with either Nikon AF Nikkor 50-mm or a wide-angle Kowa LM6HC lens. This USB3 camera has a maximum frame rate of 90 fps but can record video directly into the computer main storage (SSD). Therefore, much longer video can be obtained. Third, if full 3D particle trajectories are of interest, the Raytrix R5 plenoptic camera[20] can be used. All three cameras mentioned above have 4-megapixel light sensors. To admit only the scattered light of the illumination laser, the cameras are equipped with 660 nm bandpass interference filters with the bandwidth of 10 nm. Side-view imaging of the suspended particles is performed with the Basler acA640-100gm camera.

The top-view video of the particle suspension was analysed using the following procedure. First, we selected a region of interest at or near the center of the field of view with largest area of uniform suspension. Using ImageJ[21] software, we then cropped the video to this selected area. The particle coordinates were then calculated in each frame with subpixel resolution using a moment method[22]. The brightness of particle images was also measured and used as a proxy for their vertical position[23]. The particles were traced from frame to frame and their velocities were measured as the distance moved between two consecutive frames. The particle velocity fluctuation spectra were calculated using the method described in Ref.[20]. The transverse vertical wave spectra were calculated from the variation of the brightness of particle images[23]. The static structure factor of the particle suspension was calculated as $S(\mathbf{k}) = N^{-1}\langle\sum_{l,m} e^{i\mathbf{k}\cdot(\mathbf{r}_l-\mathbf{r}_m)}\rangle$, where N is the number of particles, $\mathbf{r}$ is the particle position, the sum runs over all pairs of particles l and m, and the averaging is performed over time.

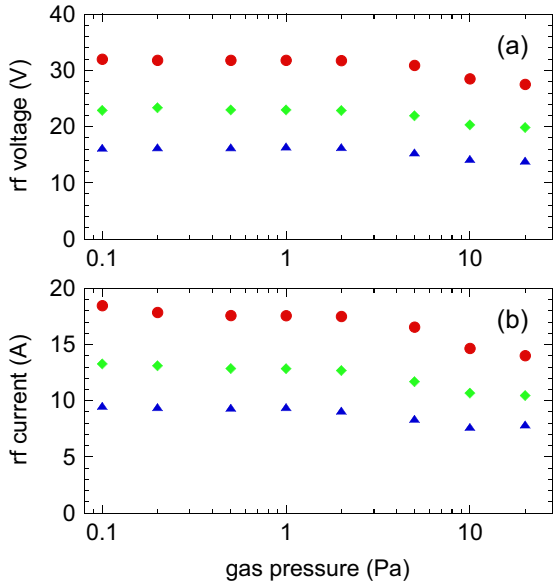

FIG. 2. Peak-to-peak amplitudes of (a) rf voltage and (b) rf current as functions of the gas pressure p_{Ar} for three different settings of the discharge power P_{rf}: 50 W (triangles), 100 W (diamonds), and 200 W (circles). The phase angle between the rf voltage and current was $\varphi \approx 70^{\circ}$.

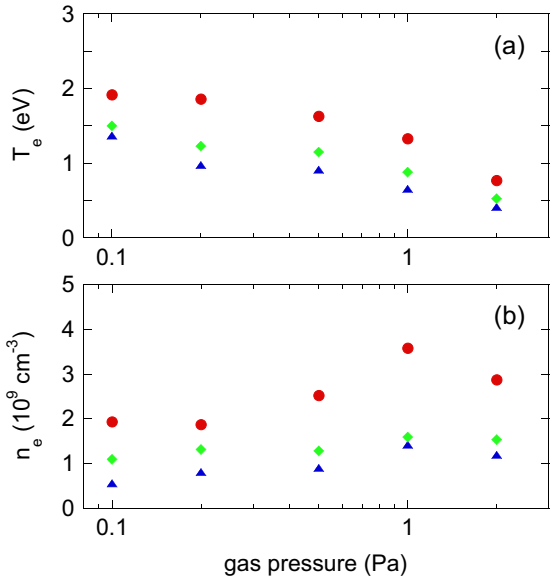

FIG. 3. (a) Electron temperature T_e and (b) electron density n_e as functions of the gas pressure p_{Ar} for three different settings of the discharge power P_{rf}: 50 W (triangles), 100 W (diamonds), and 200 W (circles). T_e and n_e were measured with a Langmuir probe in the bulk plasma 6.5 cm above the center of the rf electrode.

B. Experimental parameters and plasma diagnostics

The two most important control parameters in the complex-plasma experiments are the gas pressure and discharge power. By varying these parameters, desired experimental conditions are set for each experiment. Extensive testing of the setup showed that the practical range of the argon pressure for plasma operation is $p_{\mathrm{Ar}} =$ 0.1–20 Pa. The ultimate base pressure in the chamber is 9×10^{-4} Pa when only the smaller turbo pump is used. The practical range of the discharge forward rf power is $P_{\mathrm{rf}} =$ 5–350 W.

We measured the peak-to-peak amplitudes of the discharge rf voltage and current as functions of p_{Ar} and P_{rf} using the Solayl Vigilant rf probe[24]. The results are shown in Fig. 2. The rf voltage and current stayed more or less constant for the argon pressure in the range of 0.1 Pa $< p_{\mathrm{Ar}} <$ 5 Pa and somewhat declined for $p_{\mathrm{Ar}} \geq 5$ Pa. Compared to the GEC rf reference cell[25], the present setup is characterized by relatively high rf current and relatively low rf voltage. The latter may present an advantage in complex plasma experiments, since less sputtering of the particles and internal surfaces of the plasma chamber is expected for low discharge voltages.

To measure the basic plasma parameters, we used the Hiden ESPion rf-compensated Langmuir probe. For these measurements, the upper glass window was replaced with an aluminium flange where the probe was mounted on a vertical linear translation stage which allowed measuring the plasma parameters at different heights h_{probe} above the rf electrode. The measurements of plasma parameters for $h_{\mathrm{probe}} < 6.5$ cm or $p_{\mathrm{Ar}} \geq 5$ Pa were hindered by irregular shapes of the probe IV curves recorded in those conditions. The results of the measurements performed in the bulk plasma 6.5 cm above the center of rf electrode are shown in Fig. 3. Here, T_e was calculated from the electron retardation region of the probe characteristic and n_e from the electron saturation current evaluated at the plasma potential. At low discharge pressures like in our experiment, the electron energy distribution function (EEDF) was reported to be bi-Maxwellian[26]. Therefore, the electron temperature in Fig. 3(a) should be treated as effective temperature. As the argon pressure p_{Ar} was increased, the electron temperature T_e decreased and the electron density n_e increased, for all discharge powers used. This is a typical behaviour of rf discharges[27]. The plasma density is comparable to that achieved in experiments in the GEC setup with $p_{\mathrm{Ar}} = 2$ Pa and $P_{\mathrm{rf}} =$ 5–20 W[25]. The electron temperature T_e is lower than in the GEC setup.

III. LARGE 2D COMPLEX PLASMA CRYSTALS

To test the setup's ability to levitate dust particles, a capacitively coupled rf discharge in argon at $p_{\mathrm{Ar}} = 0.4$ Pa and $P_{\mathrm{rf}} = 150$ W was used. Dust particles were introduced into the plasma from the particle dispenser. They apparently charged up negatively and were suspended in the plasma (pre)sheath at the height of ≈ 1.5 cm above the rf electrode. The particles were levitated by the balance between the force of gravity and downward ion drag

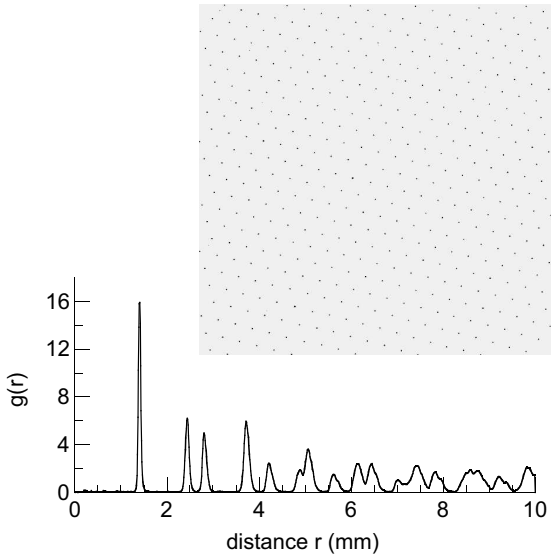

FIG. 4. (upper panel) Snapshot of a 2D complex plasma crystal showing about 400 particles and (lower panel) pair correlation function $g(r)$ for particles. The image is inverted and its brightness is adjusted for better viewing. The experimental parameters were the following: $p_{\rm Ar} = 0.4$ Pa and $P_{\rm rf} = 150$ W.

force against the upward force from the plasma sheath time-averaged electric field. In the horizontal direction, the particle confinement was provided by an aluminium-alloy ring with the internal diameter of 30 cm and height of 0.1 cm placed in the center of the rf electrode. The tilt of the whole vacuum chamber was carefully adjusted to achieve a symmetric uniform suspension of particles.

The particles self-organized into a single-layer plasma crystal with a diameter of approximately 27 cm. A central portion of the plasma crystal is shown in Fig. 4, upper panel. The particles are arranged in a triangular lattice with hexagonal symmetry. The pair correlation function $g(r)$ for particles has a narrow first peak with the magnitude of 16 and a fully split second peak, see Fig. 4, lower panel. Since the $g(r)$ of an ideal triangular lattice at zero temperature is a series of δ-functions which become broadened and can coalesce when the lattice is distorted by deformation or finite temperature[28], the $g(r)$ in Fig. 4 indicates a highly ordered lattice. The mean interparticle spacing calculated as the first peak position is 1.4 mm. Assuming the same areal number density of particles in the entire plasma crystal, the total number of particles in it is estimated as $N_p \lesssim 34000$. This plasma crystal is much larger and contains more particles then the crystals produced in previous experiments using the GEC rf reference cell[17,29,30], see Table I for comparison.

Further tests showed that stable 2D plasma crystals can be suspended in argon plasma at the pressure as low as $p_{\rm Ar} = 0.1$ Pa. The Epstein neutral gas damping rate[31] for melamine formaldehyde 9.19 μm diameter particles in argon at $p_{\rm Ar} = 0.15$ Pa is $\nu_E = 0.17$ s^{-1}. This is a small fraction ($\approx 0.5\%$) of the complex plasma's Einstein frequency[32] $\omega_E = 35$ s^{-1} in the experimental conditions of Fig. 5. Therefore, virtually undamped dynamics of complex plasma can be studied.

TABLE I. Parameters of 2D complex plasma crystals in the present work and in previous experiments using the GEC rf reference cell.

	present work	Refs.[17,29,30]
Crystal diameter (cm)	27	5–6
Number of particles	34000	5000–15000
Interparticle spacing (mm)	1.4	0.6–0.8
1$^{\rm st}$ peak of $g(r)$, magnitude	16	6–8

A. Wave modes of the plasma crystal

To characterize the dynamics of the plasma crystal, we calculated the particle velocity fluctuation spectra, see Fig. 5. The direction of the wave vector $\mathbf{k}$ was set to either $\theta = 0^\circ$ or $\theta = 90^\circ$ (measured in the crystal plane relative to the direction from a particle to the midpoint of its two nearest neighbors). The crystal's orientation angle was determined from its static structure factor $S(\mathbf{k})$.

All three dust-lattice wave modes permitted in a 2D complex plasma crystal - longitudinal in-plane (L), transverse in-plane (TH), and transverse vertical (TV) - were observed in the particle velocity fluctuation spectra. The spectra clearly have resonance nature with relatively small broadening due to low neutral-gas friction for particles. As predicted by theory[33–35] and observed in earlier experiments and simulations[23,36,37], the longitudinal and transverse in-plane modes have acoustic dispersion and the transverse vertical mode has optical dispersion. The sound speeds of the longitudinal and transverse in-plane wave modes, C_L and C_T, respectively, were calculated as the slopes of respective dispersion relations $\omega(k)$ at $k = 0$.

Two important parameters characterizing a plasma crystal are the particle charge Q and screening length λ_D. They can be inferred by fitting theoretical dispersion relations to the spectra such as those in Fig. 5; this is a commonly used and well-tested tool to study complex plasmas[34–36]. We measured the crystal spectra for various combinations of $p_{\rm Ar}$ and $P_{\rm rf}$ and in each run calculated Q and λ_D using the method of Ref.[36]. The results are presented in Fig. 6. Apparently, Q tends to become smaller as $p_{\rm Ar}$ is increased at constant $P_{\rm rf}$. Since Q is generally proportional[1] to the electron temperature T_e, the observed decrease in Q can be qualitatively explained by the underlying decrease in T_e, see Fig. 3(a). An OML theory estimate[38] of the particle charge based on the T_e measured in the bulk plasma gives $Q = 2500$–$12000e$, which is lower than the spectral-method results for the particles levitating in the plasma (pre)sheath, see Fig. 6(a). This follows the general trend of $|Q|$ getting larger when approaching the rf electrode (up to a point

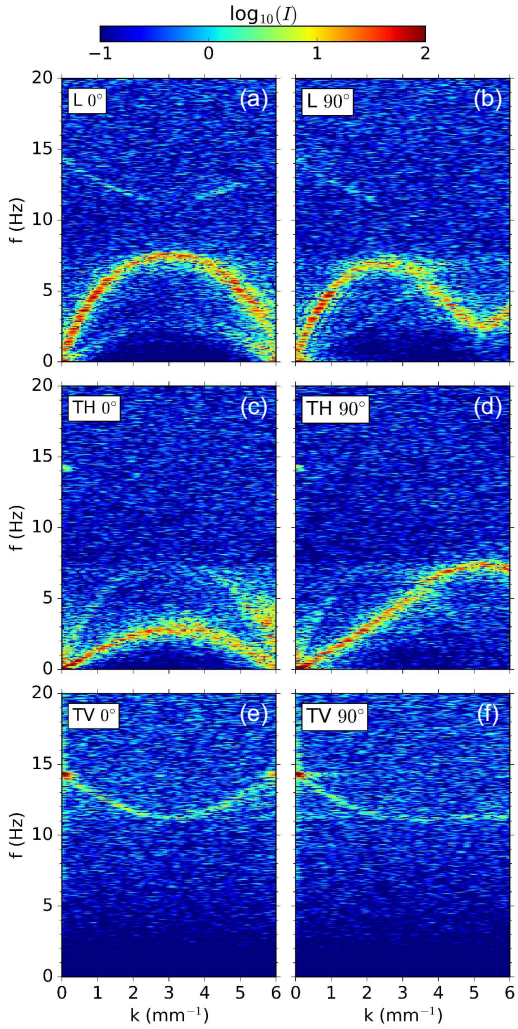

FIG. 5. Fluctuation spectra of the particle velocity showing (a),(b) longitudinal in-plane; (c),(d) transverse in-plane; and (e),(f) transverse vertical wave modes. The left column is for $\theta = 0°$, the right column for $\theta = 90°$. The following experimental parameters were used: argon pressure $p_{\rm Ar} = 0.15$ Pa and the rf power $P_{\rm rf} = 150$ W.

where $|Q|$ has its maximum)[1]. Another factor leading to the relatively high particle charge in this experiment may be the presence of additional high-temperature, low-density electron component, see discussion in Sec. II B.

Whereas there is no clear trend in λ_D with respect to the gas pressure, λ_D tends to become smaller for higher discharge power $P_{\rm rf}$. This can be explained by increasing plasma density n_e for higher $P_{\rm rf}$, see Fig. 3(b). We note that the dependence of the particle charge and screening length on experimental parameters is complicated by self-adjustment of the particle levitation height due to the balance of the sheath electrostatic force and gravity. As a result, the particle position in the plasma sheath becomes an additional factor in defining Q and λ_D, which is, however, not independent but adjusts self-consistently

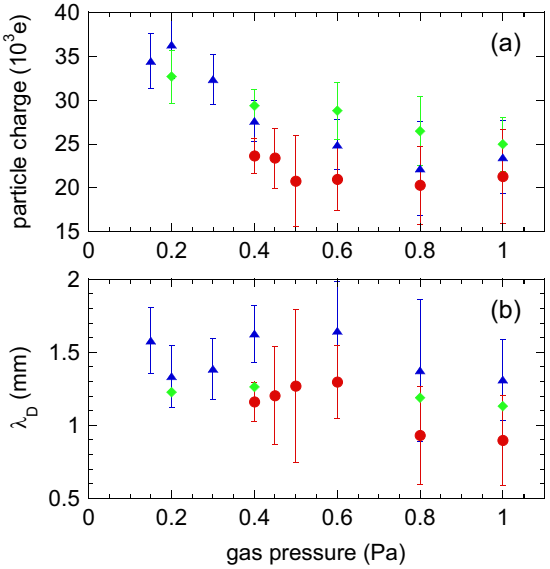

FIG. 6. (a) Particle charge Q and (b) screening length λ_D as functions of the gas pressure $p_{\rm Ar}$ for three different settings of the discharge power $P_{\rm rf}$: 50 W (triangles), 100 W (diamonds), and 200 W (circles).

to the experimental conditions. We further note that Q and λ_D in the present experiment are larger than those in typical experimental conditions in the Gaseous Electronics Conference (GEC) rf reference cell[39]. This allows one to explore complimentary parameter ranges with the new setup.

B. Mixed polarization without mode crossing

In the longitudinal in-plane spectra shown in Figs. 5(a),(b), a trace of the transverse vertical mode can be clearly seen at $f = 11$–15 Hz. This *mixed polarization* was previously believed to only occur when the L and TV modes intersect[39]. At their intersection, an unstable hybrid mode will form. If not suppressed by the gas friction, the hybrid mode will cause the so called mode-coupling instability (MCI) and eventual crystal melting[30,39,40].

In the present experiment, the mixed polarization is observed even though the modes do not cross and are separated by a frequency gap of $\simeq 4$ Hz, as was first reported in Ref.[41]. A quantitative measure of mixed polarization, defined as the ratio of the smaller to larger peak amplitudes in the intensity of the longitudinal spectrum averaged in the range $1.4\ {\rm mm}^{-1} < |k| < 1.8\ {\rm mm}^{-1}$, is 0.07 ± 0.04 for $\theta = 0°$ and 0.06 ± 0.03 for $\theta = 90°$. Notice the apparent asymmetry in the mixed polarization: there is no evidence of a trace of the L mode in the TV mode spectra shown in Figs. 5(e) and 5(f). This kind of mixed polarization may not have been resolved due to insufficient signal-to-noise ratio in the TV spectra.

To rule out a mere geometric effect (e.g., the camera perspective[42]) as a possible trivial reason for the appear-

ance of mixed polarization, molecular dynamics simulations and theoretical analysis were performed in Ref.[41]. Both simulations and theoretical analysis were based on solving the equations of motion for particles confined by external potential, with the following forces taken into account: pairwise Yukawa interparticle interaction, the neutral gas drag force, and the Langevin force providing a heat bath. Ion wakes beneath the negatively charged particles were modeled as positive pointlike charges placed a fixed distance below each particle. In the simulations, the geometric effect was not present by design; however, the mixed polarization was observed as in the experiment. The theoretical analysis of the coupled modes matched the simulation and the experiment. Therefore, the mixed polarization observed in the experiments is a genuine result of coupling between the non-crossing modes.

Theory predicts that the mixed polarization can only be significant for relatively large ion wake charges[41]. The small damping rate due to low gas pressure and high crystal quality in the present experiment are other reasons why the observation of the mixed polarization without mode crossing became possible in the new experimental setup.

IV. CONCLUSIONS AND OUTLOOK

To summarize, new experimental setup for studying large 2D complex plasma crystals was built at the DLR Institute of Materials Physics in Space. A capacitively coupled rf discharge in a stainless-steel chamber with external diameter of 90 cm is used to levitate dust particles in the plasma sheath above the lower rf electrode. In test runs, single-layer complex plasma crystals with a diameter of ≈ 27 cm and total number of particles ≈ 34000 were suspended. The crystals were highly ordered. All three principal wave modes allowed in 2D plasma crystals were observed, their spectra had clear resonance nature. Mixed polarization of the longitudinal in-plane and transverse vertical wave modes was observed in experimental conditions where the modes did not cross.

The new setup allows to explore extended parameter ranges, in particular, stable 2D plasma crystals can be obtained at a gas pressure as low as 0.1 Pa. This allows to study the plasma crystal dynamics in virtually undamped regime.

Experiments with even larger 2D complex plasma crystals are planned. Future work will explore the system-size dependence of selected plasma crystal properties, e.g. viscosity and thermal conductivity.

ACKNOWLEDGMENTS

The authors thank Heinrich Huber, Hermann Kronbauer, Johannes Prell, Alexander Börngen, Sebastian Peralta Friedburg, and Claudius George for their valuable help in designing and building the experimental setup reported in this paper and Christina Knapek for carefully reading the manuscript. This work received funding from the Bavarian StMWi. J. M. acknowledges the support of DLR-DAAD Research Fellowships.

[1] A. Ivlev, H. Löwen, G. Morfill, C. P. Royall, *Complex Plasmas and Colloidal Dispersions: Particle-resolved Studies of Classical Liquids and Solids*, Series in Soft Condensed Matter Vol. 5 (World Scientific, Singapore, 2012).
[2] H. Thomas, G. E. Morfill, V. Demmel, J. Goree, B. Feuerbacher, and D. Möhlmann, Phys. Rev. Lett. **73**, 652 (1994).
[3] Y. Hayashi and K. Tachibana, Jpn. J. Appl. Phys. **33**, L804 (1994).
[4] J. H. Chu and I Lin, Phys. Rev. Lett. **72**, 4009 (1994).
[5] V. Nosenko, A. V. Ivlev, G. E. Morfill, Phys. Rev. Lett. **108**, 135005 (2012).
[6] S. Nunomura, J. Goree, S. Hu, X. Wang, A. Bhattacharjee, and K. Avinash, Phys. Rev. Lett. **89**, 035001 (2002).
[7] A. Piel, V. Nosenko, J. Goree, Phys. Rev. Lett. **89**, 085004 (2002).
[8] S. K. Zhdanov, S. Nunomura, D. Samsonov, and G. Morfill, Phys. Rev. E **68**, 035401 (2003).
[9] K. Avinash, P. Zhu, V. Nosenko, and J. Goree, Phys. Rev. E **68**, 046402 (2003).
[10] H. M. Thomas and G. E. Morfill, Nature (London) **379**, 806 (1996).
[11] V. Nosenko, S. K. Zhdanov, A. V. Ivlev, C. A. Knapek, and G. E. Morfill, Phys. Rev. Lett. **103**, 015001 (2009).
[12] A. Melzer, A. Schella, J. Schablinski, D. Block, and A. Piel, Phys. Rev. E **87**, 033107 (2013).
[13] S. Nunomura, D. Samsonov, S. Zhdanov, and G. Morfill, Phys. Rev. Lett. **96**, 015003 (2006).
[14] V. Nosenko and J. Goree, Phys. Rev. Lett. **93**, 155004 (2004).
[15] A. Gavrikov, I. Shakhova, A. Ivanov, O. Petrov, N. Vorona, and V. Fortov, Phys. Lett. A **336**, 378 (2005).
[16] P. Hartmann, M. C. Sándor, A. Kovács, and Z. Donkó, Phys. Rev. E **84**, 016404 (2011).
[17] V. Nosenko, S. K. Zhdanov, A. V. Ivlev, G. E. Morfill, J. Goree, and A. Piel, Phys. Rev. Lett. **100**, 025003 (2008).
[18] P. J. Hargis, K. E. Greenberg, P. A. Miller *et al.*, Rev. Sci. Instrum. **65**, 140 (1994).
[19] Marketed by Microparticles GmbH, see http://microparticles.de.
[20] M. Jambor, V. Nosenko, S. K. Zhdanov, and H. M. Thomas, Rev. Sci. Instrum. **87**, 033505 (2016).
[21] https://imagej.net/Welcome.
[22] U. Konopka (unpublished).
[23] L. Couëdel, V. Nosenko, S. K. Zhdanov, A. V. Ivlev, H. M. Thomas, and G. E. Morfill, Phys. Rev. Lett. **103**, 215001 (2009).
[24] Marketed by Solayl, see https://www.solayl.com/.
[25] V. Nosenko, A. V. Ivlev, R. Kompaneets, and G. Morfill, Phys. Plasmas **21**, 113701 (2014).
[26] V. A. Godyak, R. B. Piejak, and B. M. Alexandrovich, J. Appl. Phys. **73**, 3657 (1993).
[27] V. A. Godyak and V. I. Demidov, J. Phys. D: Appl. Phys. **44**, 233001 (2011).
[28] R. A. Quinn, C. Cui, J. Goree, J. B. Pieper, H. Thomas, and G. E. Morfill, Phys. Rev. E **53**, R2049 (1996).
[29] V. Nosenko, J. Goree, and A. Piel, Phys. Plasmas **13**, 032106 (2006).
[30] L. Couëdel, V. Nosenko, A. V. Ivlev, S. K. Zhdanov, H. M. Thomas, and G. E. Morfill, Phys. Rev. Lett. **104**, 195001 (2010).
[31] B. Liu, J. Goree, and V. Nosenko, Phys. Plasmas **10**, 9 (2003).
[32] C. A. Knapek, A. V. Ivlev, B. A. Klumov, G. E. Morfill, and D. Samsonov, Phys. Rev. Lett. **98**, 015001 (2007).
[33] S. V. Vladimirov, P. V. Shevchenko, and N. F. Cramer, Phys. Rev. E **56**, R74 (1997).
[34] X. Wang, A. Bhattacharjee, and S. Hu, Phys. Rev. Lett. **86**, 2569 (2001).
[35] S. K. Zhdanov, A. V. Ivlev, and G. E. Morfill, Phys. Plasmas **16**, 083706 (2009).

[36] S. Nunomura, J. Goree, S. Hu, X. Wang, A. Bhattacharjee, Phys. Rev. E **65**, 066402 (2002).
[37] K. Qiao and T. W. Hyde, Phys. Rev. E **68**, 046403 (2003).
[38] M. Bonitz, C. Henning, and D. Block, Rep. Prog. Phys. **73**, 066501 (2010).
[39] L. Couëdel, S. K. Zhdanov, A. V. Ivlev, V. Nosenko, H. M. Thomas, and G. E. Morfill, Phys. Plasmas **18**, 083707 (2011).
[40] A. V. Ivlev and G. Morfill, Phys. Rev. E **63**, 016409 (2001).
[41] J. K. Meyer, I. Laut, S. K. Zhdanov, V. Nosenko, H. M. Thomas, Phys. Rev. Lett. **119**, 255001 (2017).
[42] When observing the plasma crystal not perfectly from above but at an angle, the vertical particle displacement is also projected onto the measured in-plane displacement.